
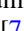


Pathway to chaos through hierarchical superfluidity in blue-detuned cavity-BEC systems

Rui Lin ¹, Paolo Mognini,^{1,2} Axel U. J. Lode ³, and R. Chitra¹

¹*Institute for Theoretical Physics, ETH Zurich, 8093 Zurich, Switzerland*

²*Clarendon Laboratory, University of Oxford, Parks Road, Oxford OX1 3PU, United Kingdom*

³*Institute of Physics, Albert-Ludwig University of Freiburg, Hermann-Herder-Straße 3, 79104 Freiburg, Germany*



(Received 8 October 2019; revised manuscript received 25 May 2020; accepted 28 May 2020; published 30 June 2020)

We explore the role of atomic correlations in a harmonically trapped Bose-Einstein condensate coupled to a dissipative cavity where both the atoms and the cavity are blue-detuned from the external pumping laser. Using a genuine beyond-mean-field many-body approach, we extract density distributions and many-body correlations to unveil a pathway to chaos at large pump power through a hierarchical self-organization of the atoms where the atoms transition from a single-well optical lattice to a double-well optical lattice. Correlated states of the atoms emerge and are characterized by local superfluid correlations in phases which are globally superfluid or Mott insulating. Local superfluid-Mott transitions are precluded by a dynamical instability to chaos which occurs via quasiperiodic attractors. Our results explain the mechanism behind the dynamical instabilities observed in experiments.

DOI: [10.1103/PhysRevA.101.061602](https://doi.org/10.1103/PhysRevA.101.061602)

Introduction. Experimental advances in the past decade have heralded a new era in light-matter hybrid systems where quantum light is used to engineer correlated phases of matter. In the solid-state realm, coupling to light has been used to activate phases of matter, such as ferroelectricity [1] and superconductivity [2]. In the quantum engineering domain, cavity-QED systems with their tunable light-matter couplings provide a versatile platform to realize hybrid correlated quantum fluids, such as polaritons [3,4], permit the encoding of qubits through photons [5], and generate entangled quantum many-body states for quantum computation [6].

A landmark example of a light-induced phase is super-radiance [7–10] in strongly coupled cavity-Bose-Einstein condensate (BEC) systems where the atoms in the BEC self-organize onto a lattice dynamically generated by the cavity field [11–13]. Cavity-BEC systems also host complex phases, such as Mott insulators [14–18], supersolids [19–21], and spin textures [22–26]. They additionally allow the simulation of many-body Hamiltonians having no solid-state counterparts, such as spin models with both short- and long-range interactions [2,27], and the realization of exotic collective magnetic phenomena [28].

Prior theoretical work highlighted the ability of blue-detuned cavity-atom systems to stabilize limit cycles and chaos [30,31]. Although the predicted limit cycles were not seen in the first experimental study of this regime, interesting dynamical instabilities were reported [32]. Motivated by this study, we go beyond Refs. [30,31] and explore the atomic correlations and dynamical instabilities in a realistic harmonically trapped cavity-BEC system [Fig. 1(a)] and map the rich phase diagram in Fig. 1(b). On the pathway to chaos, we reveal an unexpected hierarchical deformation of the optical lattice into a double-well lattice, which generates new correlated phases of the atoms. In the dynamically unstable regime, we also observe that quasiperiodicity dominates instead of strict

periodicity, which is compatible to experiments. Our proposed phase diagram and methodology are relevant for different experimental realizations, such as in Refs. [12,14,33].

Model and method. We consider a cavity-BEC system with N bosonic atoms of mass m . From a computational perspective since the physics of the system does not qualitatively depend on the dimensionality, we study a one-dimensional version of the model and later discuss the validity of the results obtained for the two-dimensional system. In the rotating frame of the pump laser, the system is described by the following coupled equations of motion for the cavity expectation value α and the atomic field operators $\hat{\Psi}^{(\dagger)}(x)$ [11,34]:

$$i \partial_t \hat{\Psi}(x) = \left[-\frac{\hbar \partial_x^2}{2m} + \frac{g}{\hbar} \hat{\Psi}^\dagger(x) \hat{\Psi}(x) + \frac{1}{\hbar} V_{\text{trap}}(x) + U_0 \cos^2(k_c x) |\alpha|^2 + \eta \cos(k_c x) (\alpha + \alpha^*) \right] \hat{\Psi}(x). \quad (1a)$$

$$\partial_t \alpha = (i \Delta_c - i N U_0 B - \kappa) \alpha - i \eta N \theta. \quad (1b)$$

Here, k_c is the wave vector of the cavity field and corresponds to the recoil frequency $\omega_R \equiv \hbar k_c^2 / 2m$. g is the weak interatomic interaction, U_0 is the atomic single-photon light shift, η is the effective pump rate, Δ_c is the cavity detuning, and κ is the cavity dissipation rate. The blue-detuning of atoms and cavity is reflected in U_0 and Δ_c being positive, respectively. The atoms are confined by a harmonic trap $V_{\text{trap}}(x) = \frac{m}{2} \omega_x^2 x^2$. Since we are interested in regimes far from the normal-superradiant boundary, the cavity is in a coherent state with negligible fluctuations [18,35–37] and can, thus, be represented by a complex number α . The variables $\theta = \int dx \rho(x) \cos(k_c x)$ and $B = \int dx \rho(x) \cos^2(k_c x)$ in Eq. (1b) are the order parameters

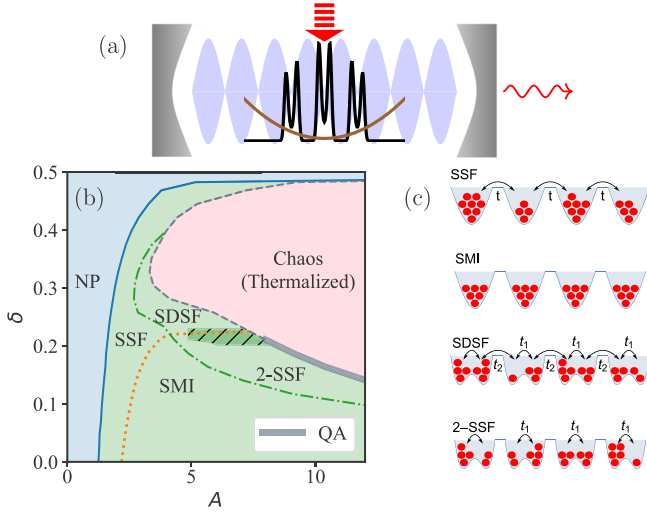


FIG. 1. (a) Schematic of a trapped cavity-BEC. (b) Phase diagram. For cavity detuning $0 < \delta < 1/2$, the system transitions from the normal phase (NP) to the dynamically unstable region via superradiance with increasing pump rate $A \propto \eta$. The strongly correlated phases are a self-organized superfluid (SSF), a self-organized Mott insulator (SMI), a self-organized dimerized superfluid (SDSF), and a self-organized second-order superfluid (2-SSF) phase. The orange dotted line separates superfluid phases and globally Mott insulating phases, whereas the green dash-dotted line marks the onset of the hierarchical self-organization to dimerized phases. Pronounced sensitivity to the ramping protocol is seen in the hatched dark green region. At higher A , the system is dynamically unstable to the formation of quasiperiodic attractors (QA) followed by chaos. The QAs only exist in the region represented by the thick gray line, whereas the thin dashed section represents a direct transition to the chaos. The dimensionless detuning δ and the potential strength A are normalized with respect to NU_0 and $\sqrt{\omega_R}$, respectively [see Eq. (2)]. (c) Sketch of the SSF, SMI, SDSF, and 2-SSF phases.

associated with superradiance, where $\rho(x) = \langle \hat{\Psi}^\dagger(x)\hat{\Psi}(x) \rangle / N$ is the position space density distribution.

The main characteristic features of the system are direct results of the cavity-induced potential. For our analytical considerations, we neglect the atomic interactions, atomic correlations, and the harmonic trap and adiabatically eliminate the cavity field via setting $\partial_t \alpha = 0$. We find that the atoms are effectively subject to the potential [11],

$$V_{\text{cav}}(x) = A^2 \hbar \omega_R [2(\delta - B)\theta \cos(k_c x) + \theta^2 \cos^2(k_c x)], \quad (2)$$

with $A = \eta N \sqrt{U_0} / \sqrt{[(\Delta_c - NU_0 B)^2 + \kappa^2] \omega_R}$ as the dimensionless overall effective potential strength and $\delta = \Delta_c / NU_0$ as the dimensionless cavity detuning. The cavity dynamically creates an optical lattice potential comprising two sinusoidal terms $\cos^2(k_c x)$ and $\cos(k_c x)$, whose amplitudes are determined by the instantaneous atomic state via θ and B .

With blue-detuned atoms $U_0 > 0$, self-organization takes place in both a red-detuned cavity $\delta < 0$ and a blue-detuned cavity $0 < \delta < 1/2$ [11,12,38]. In the former case, the $\cos(k_c x)$ term dominates, and the atoms are localized at the lattice sites $x_n = n\pi/k_c$ with all n either even or odd. However, in the latter case, the two terms in V_{cav} can be equally significant, forming a local double well at each site. This

double-well lattice can realize the Su-Schrieffer-Heeger model in a cavity-fermion system [39]. This analysis provides the first glimpse of intrinsically different physics in the blue-detuned region.

Most phenomena in the blue-detuned cavity-BEC system, including the atomic self-organization, the double-well lattice, and the dynamical instabilities, can be revealed by the system's evolution in the (B, θ) phase space in discretized time. This evolution can be found by noting that the instantaneous potential [Eq. (2)] is controlled by the two order parameters from the past step (B_t, θ_t) and, subsequently, determines the quantum state and, thus, the parameters in the next step (B_{t+1}, θ_{t+1}) . Using a Gaussian ansatz for the quantum states, the two parameters are found to evolve as follows:

$$\theta_{t+1} = e^{-1/4\Omega_t} \chi_t, \quad B_{t+1} = \frac{1}{2} + \frac{1}{2} e^{-1/\Omega_t} (2\chi_t^2 - 1), \quad (3a)$$

with

$$\Omega_t = \begin{cases} A\sqrt{|\theta_t|(B_t - \delta - |\theta_t|)/2}, & B_t - \delta \geq |\theta_t|, \\ A\sqrt{[\theta_t^2 - (\delta - B_t)^2]/2}, & B_t - \delta < |\theta_t| \end{cases} \quad (3b)$$

$$\chi_t = \begin{cases} \text{sgn}(\theta_t), & B_t - \delta \geq |\theta_t| \\ (B_t - \delta)/\theta_t, & B_t - \delta < |\theta_t|. \end{cases} \quad (3c)$$

Beyond the mean-field limit, the combination of the double-well optical lattice and weak atomic interactions results in hierarchical transitions to a series of correlated phases of matter. We investigate the full phase diagram described by Eq. (1) using the multiconfigurational time-dependent Hartree method for indistinguishable particles (MCTDH-X) [40–45]. The simulated $N = 50$ atoms are initialized in a Thomas-Fermi-like state. Then the many-body state of the atoms coupled to the cavity is propagated in real time. The pump rate η is linearly ramped up at fixed detunings to reach a desired value. The simulation parameters correspond to those realized experimentally in Ref. [12] and are given in detail in the Supplemental Material [29].

The phase diagram is extracted from the observables: θ , B , the position space density distribution $\rho(x)$, the momentum space density distribution $\tilde{\rho}(k) = \langle \hat{\Psi}^\dagger(k)\hat{\Psi}(k) \rangle / N$, and the Glauber one-body correlation function $g^{(1)}(x, x') = \langle \hat{\Psi}^\dagger(x)\hat{\Psi}(x') \rangle / \sqrt{N^2 \rho(x)\rho(x')}$ [46,47], whose behaviors are summarized in Fig. 2. The simulation results from MCTDH-X will be compared to the analytical results from Eq. (3) (see Fig. 3).

Results. Our results for the blue-detuned cavity-BEC are summarized in the phase diagram [Fig. 1(b)] along with a schematic of the different phases [Fig. 1(c)]. The system self-organizes at a critical pump rate η_c roughly consistent with the mean-field prediction $A(\eta_c) = 1/\sqrt{1 - 2\delta}$ [11]. We plot $\rho(x)$ and $\tilde{\rho}(k)$ at two representative detunings in Figs. 2(a)–2(d). The self-organized superfluid (SSF) phase is characterized by a continuous density distribution $\rho(x)$ with pronounced peaks at the sites of the emergent lattice with spacing $\lambda_c = 2\pi/k_c$. The corresponding $\tilde{\rho}(k)$, measurable by time-of-flight experiments, is characterized by a principal peak at the center $k = 0$ straddled by two satellite peaks at $k = \pm k_c$ stemming from the superfluid correlations between the atoms at different lattice sites [14,17,18]. At lower detunings $\delta \lesssim 0.2$ and larger pump rate, the system transitions from the superfluid into

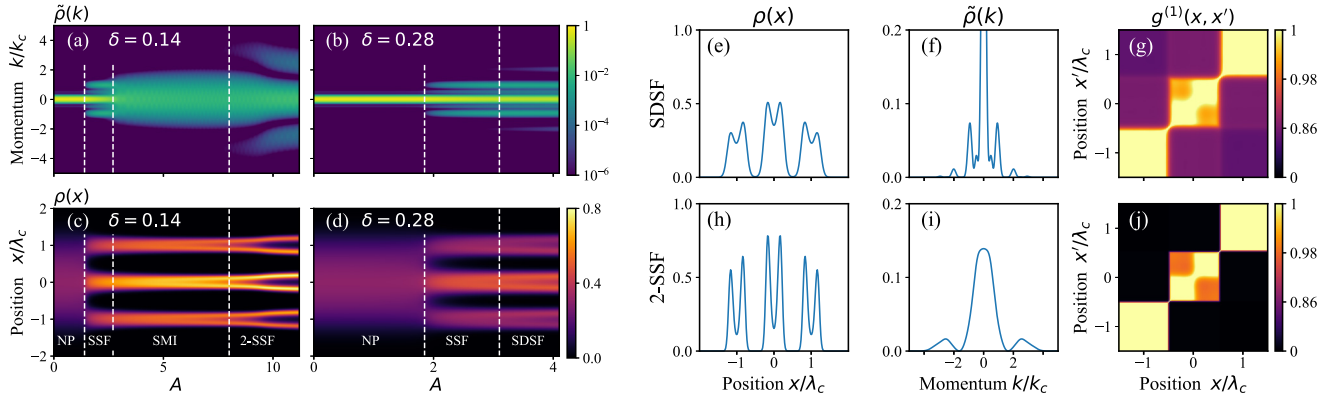


FIG. 2. (a)–(d) The momentum and position space density distributions $\tilde{\rho}(k)$ and $\rho(x)$ as a function of pump rate $A \propto \eta$ at two detunings $\delta = 0.14$ and $\delta = 0.28$. At lower detuning $\delta = 0.14$, the system starts from the normal phase and then enters the SSF phase at $A = 1.4$, the SMI phase at $A = 2.7$, and the 2-SSF phase sequentially. At higher detuning $\delta = 0.28$, the system starts from the normal phase, then enters the SSF phase at $A = 1.9$, and the SDSF phase sequentially. The dotted lines are guides to the eye. (e)–(j) The position and momentum space density distributions and the Glauber one-body correlation function of an SDSF state (first row) and a 2-SSF state (second row). In panels (g) and (j), the color code follows the function $-\ln(1 - g^{(1)})$. The double-well splitting is seen in the central lattice site but not in the other two lattice sites because only $M = 4$ orbitals are used in the numerical simulations (see the Supplemental Material [29]).

a self-organized Mott insulator (SMI) phase. This phase is characterized by the disappearance of the peaks at $k = \pm k_c$ and the broadening of the central peak at $k = 0$ in $\tilde{\rho}(k)$ [14,18,48–50]. These superfluid and Mott insulating phases are analogs to the ones in a standard Bose-Hubbard model [18]. In the (B, θ) phase space, these two phases with single-well lattices are characterized by stable fixed points with $B - \delta > |\theta|$ [Figs. 3(b) and 3(g)]. Such phases always appear first as A passes a critical value and the system leaves the normal phase ($B = 1/2, \theta = 0$) [Figs. 3(a) and 3(f)].

As the pump rate increases further, the fixed point moves in phase space. As $B - \delta$ becomes smaller than $|\theta|$ [Figs. 3(c) and 3(h)], local double-well potentials are formed at lattice sites according to Eq. (2). This is unique to blue-detuned systems. Depending on the degree of correlations between the atoms at different sites, we obtain either a self-organized dimerized superfluid (SDSF) phase where global superfluid correlations persist across the double-well dimers or a self-

organized second-order superfluid (2-SSF) phase where superfluid correlations exist only within each double-well dimer. The signatures of these two states lie in the distributions $\rho(x)$ and $\tilde{\rho}(k)$ and the correlation function $g^{(1)}(x, x')$ as shown in Figs. 2(e)–2(j). The double-well optical lattice is confirmed by the two-humped density distribution in $\rho(x)$ at each lattice site [Figs. 2(e) and 2(h)] and the concomitant reduction of the one-body correlation from unity within one lattice site [Figs. 2(g) and 2(j)]. Within each double-well dimer, local superfluidity exists and manifests itself as two peaks in $\tilde{\rho}(k)$ appearing at $k = \pm k^*$ [Figs. 2(f) and 2(i)], where

$$k^* = \frac{\pi k_c}{\arccos[(B - \delta)/|\theta|]} \quad (4)$$

corresponds to the distance between the minima of the double-well potential. As the pump rate increases, k^* approaches $2k_c$ from above, and the peak height increases as the double well becomes deeper.

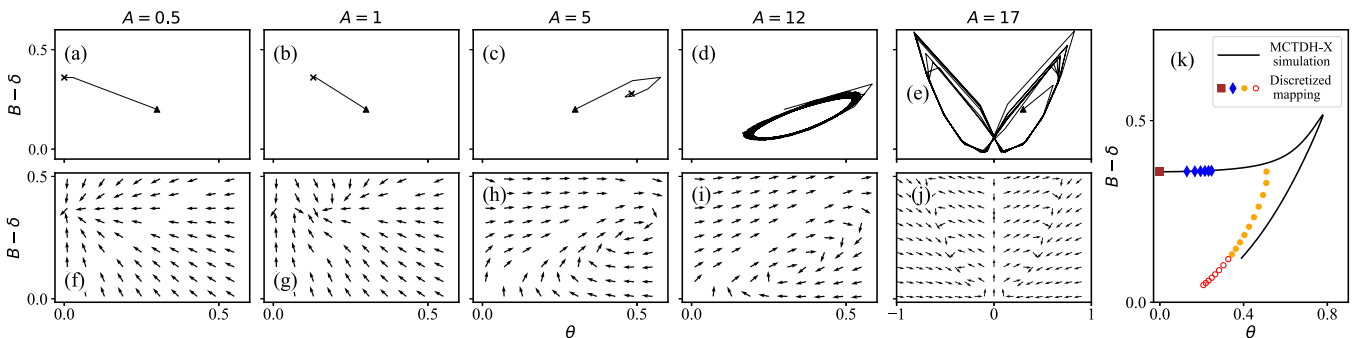


FIG. 3. (a)–(e) The trajectory of the parameter pair (B, θ) on phase space evolving according to Eq. (3) with randomly chosen initial values marked by triangles and fixed points marked by crosses. (f)–(j) The corresponding flow vector plots with normalized arrows showing only the flow directions. In all panels, we choose $\delta = 0.14$. As A increases, the system is in (a) and (f) a normal phase at $A = 0.5$, (b) and (g) a single-well lattice at $A = 1$, (c) and (h) a double-well lattice at $A = 5$, (d) and (i) an attractor phase at $A = 12$, and (e) and (j) chaos at $A = 17$. (k) The trajectory of the fixed points as A changes. The solid brown square, blue diamonds, and orange points are stable fixed points for NP, single-well lattices, and double-well lattices, respectively. The red empty points show the unstable fixed points. A black line is superposed to show the trajectory in the MCTDH-X simulation in dynamically stable phases.

In the SDSF (2-SSF) phase, global superfluid correlations between different pairs of double wells are present (absent). This corresponds to the presence (absence) of the peaks at k_c in $\tilde{\rho}(k)$ [Figs. 2(f) and 2(i)], and a finite (vanishing) correlation in $g^{(1)}$ between different lattice sites [Figs. 2(g) and 2(j)]. In a 2-SSF state, superfluidity has a completely different length scale from the SSF and SDSF states since coherence exists only locally within each double-well dimer. Although superfluidity usually refers to long-range coherence, it can also be used to describe coherence within a double well [51]. These two new phases realize a variant of the Bose-Hubbard model with degenerate double-well lattices with Hamiltonian,

$$\hat{H}_{\text{BH}} = - \sum_i (t_1 \hat{c}_{i,L}^\dagger \hat{c}_{i,R} + t_2 \hat{c}_{i,R}^\dagger \hat{c}_{i+1,L} + \text{H.c.}) + \sum_{i,\sigma=L,R} \left[\frac{U}{2} (\hat{c}_{i,\sigma}^\dagger \hat{c}_{i,\sigma})^2 + \mu_i \hat{c}_{i,\sigma}^\dagger \hat{c}_{i,\sigma} \right], \quad (5)$$

where L,R denote the subsites, U the on-site atomic interaction, μ_i the local chemical potential, and t_1 and t_2 the intra-dimer and inter-dimer hoppings, respectively [52].

The single-well optical lattice smoothly deforms to the double-well lattice, and it is hard to numerically establish if the system transitions or crosses over during the dimerization (see the Supplemental Material [29]). Nonetheless, clear hysteretic behavior is seen across the boundary between SDSF and 2-SSF phases, shown by the hatched dark green region in Fig. 1(b). This implies a first-order transition between the globally superfluid and the globally Mott insulating phases.

At higher pump rates, the fixed points of Eq. (3) become unstable through a Hopf bifurcation [53,54] as attested by the trajectory and flow in Figs. 3(d) and 3(i), and the appearance of dynamical instabilities in the cavity-BEC system. Such instabilities preclude Mott insulation within a double well [Fig. 1(b)]. In the presence of the atomic interactions and the harmonic trap, the limit cycles predicted in a noninteracting trapless system [30,31] are reduced to quasiperiodic attractors (QAs). Similar to the limit cycles, the QAs are shown to be robust against ramping protocols in Figs. 4(a) and 4(b): The trajectories are always confined in the same region in the (B, θ) phase space [Fig. 4(b)], and they exhibit roughly the same amplitude and frequency profile of oscillations [Fig. 4(a)]. In contrast to limit cycles, QAs are highly sensitive to initial conditions, reflecting their connection to chaos. Nevertheless, the double-well configuration of the atomic density is well preserved in a QA state [Fig. 4(c)].

As the pump rate further increases, the discretized-time model predicts θ , and thereby the optical lattice will repeatedly vanish transiently [Figs. 3(e) and 3(j)]. In the cavity-BEC system, the atoms become loosely confined, and higher momentum modes are easily excited, leading to a rapid increase in system energy and resulting in full chaos and thermalization [Fig. 4(d)]. In this thermalized regime, the atomic density distribution eventually becomes completely fluctuative, and the system becomes fully chaotic [Fig. 4(c)]. Tightly trapped systems are more prone to thermalization (see the Supplemental Material [29]).

Discussion and extension to two-dimensional systems. In terms of the renormalized parameters δ and A [cf. Eq. (2)], the phase diagram is rather general and relevant for multiple

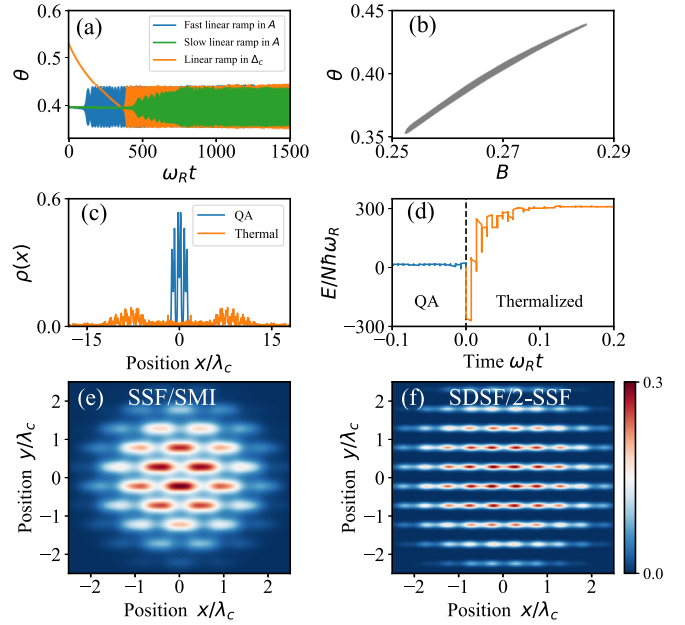


FIG. 4. (a) The order parameter θ as a function of time for three different ramping protocols from the stable region into the QA phase ($\delta = 0.14$, $A = 11.8$). In the blue and green trajectories, the detuning is fixed at $\delta = 0.14$, and the pump rate $A \propto \eta$ is ramped up linearly at rates of (blue) $dA/dt = 4 \times 10^{-4} \omega_R$ and (green) $dA/dt = 8 \times 10^{-5} \omega_R$, respectively. In the orange trajectory, the pump rate is fixed at $A = 11.8$, and the detuning is ramped up linearly at a rate of $d\delta/dt = 1.5 \times 10^{-4} \omega_R$. (b) For all three cases, the system converges to the same attractor in the (B, θ) phase space. (c) Density distribution $\rho(x)$ of (blue) a QA state and (orange) a thermalized state. (d) Evolution of the system energy as the system becomes thermalized. The reference time $t = 0$ is set roughly when the thermalization starts. (e) and (f) The position space density distribution $\rho(x, y)$ of (e) a single-well lattice state and (f) a double-well lattice state in a two-dimensional cavity-BEC system as described by Eq. (6).

experimental setups [12,33,55]. At the mean-field level, we have seen that the discretized mapping Eq. (3) qualitatively predicts various phenomena observed in simulations. In addition, its fixed points also roughly track the simulated system trajectory in phase space [Fig. 3(k)].

We now discuss the dependence of the phase diagram on the atom number N and the trap. There are two kinds of phase boundaries in Fig. 1(b): the mean-field ones, and the nonmean-field ones. The first kind (self-organization and dynamical stability boundaries) is governed by the cavity-induced effective potential in Eq. (2), which solely depends on δ and A . Thus, these phase boundaries, given as functions of δ and A , remain unchanged for any particle number and are only weakly sensitive to the trap [18]. The second kind delineates the phases SSF, SMI, 2-SSF and SDSF. These transitions are driven by Bose-Hubbard physics and are determined by the filling factor at lattice sites. As N increases and the harmonic trap tightens, the filling factor increases and these phase boundaries move towards larger A . Based on these observations, we have made a computationally judicious choice of particle number and trapping frequency to effectively simulate the experimentally relevant phase diagram.

The phase diagram for the one-dimensional system can be straightforwardly extended to the experimentally relevant two-dimensional systems. In this case, the atoms are subject to three light-induced effective potentials which we require to be as follows:

$$V_{\text{light}}(x, y) = \hbar\eta^2/U_0 \cos^2(k_c y) + \hbar U_0 |\alpha|^2 \cos^2(k_c x) + \hbar\eta(\alpha + \alpha^*) \cos(k_c x) \sin(k_c y). \quad (6)$$

Compared to the one-dimensional version [Eq. (1a)], the first term is an additional term stemming from the transverse pumping laser. The cavity field α follows the equation of motion Eq. (1b) where the lattice order parameter is generalized to $\theta = \int dx dy \langle \hat{\Psi}^\dagger(x, y) \hat{\Psi}(x, y) \rangle \cos(k_c x) \sin(k_c y) / N$. Compared to the effective potential realized very recently in experiment [32], the essential difference in the above system [Eq. (6)] is an extra phase shift of $\pi/2$ along the pump (y) axis in the last term. This phase shift is necessary to observe our phase diagram and can straightforwardly be implemented in the experimental setup.

The two-dimensional system is expected to qualitatively possess the same phase diagram shown in Fig. 1(b). All the phases should be accessible for reasonable values of the detuning and pump rate. In Figs. 4(e) and 4(f), we plot two representative examples of spatial density distributions based

on mean-field simulations, (i) the standard self-organization on a checkerboard lattice corresponding to an SSF or an SMI, and (ii) self-organization on the double-well optical lattice structures. The latter would lead to extra peaks in momentum space at $\mathbf{k} = (\pm k^*, 0)$ superposed over the underlying superfluid or Mott-insulator momentum distribution, which can serve as the smoking-gun evidence of dimerization in experiment. The oscillatory phase reminiscent of our quasiperiodic attractors has already been observed experimentally [32]. Despite the phase shift between the experimental setup and the one discussed in this Rapid Communication, we expect the same mechanism driving the dynamical instabilities. To clearly observe the quasiperiodicity in an experiment, a loose trap along the cavity axis with $\omega_x \sim 10^{-3} \omega_R$ is suggested (see the Supplemental Material [29]).

Our Rapid Communication illustrates the potential of blue detuning to realize exotic phases of matter and should stimulate future studies of complex cavity-cold atom platforms.

Acknowledgments. We acknowledge the financial support from the Swiss National Science Foundation (SNSF), the ETH Grants, G. Anderheggen, and the Austrian Science Foundation (FWF) under Grant No. P32033. We also acknowledge the computation time on the ETH Euler cluster and the Hazel Hen Cray cluster at the HLRS Stuttgart.

-
- [1] P. Zalden, F. Quirin, M. Schumacher, J. Siegel, S. Wei, A. Koc, M. Nicoul, M. Trigo, P. Andreasson, H. Enquist *et al.*, *Science* **364**, 1062 (2019).
- [2] F. Schlawin, A. Cavalleri, and D. Jaksch, *Phys. Rev. Lett.* **122**, 133602 (2019).
- [3] P. Knüppel, S. Ravets, M. Kroner, S. Fält, W. Wegscheider, and A. Imamoglu, *Nature (London)* **572**, 91 (2019).
- [4] S. Latini, E. Ronca, U. De Giovannini, H. Hübener, and A. Rubio, *Nano Lett.* **19**, 3473 (2019).
- [5] M. Körber, O. Morin, S. Langenfeld, A. Neuzner, S. Ritter, and G. Rempe, *Nat. Photonics* **12**, 18 (2018).
- [6] S. Welte, B. Hacker, S. Daiss, S. Ritter, and G. Rempe, *Phys. Rev. X* **8**, 011018 (2018).
- [7] R. H. Dicke, *Phys. Rev.* **93**, 99 (1954).
- [8] K. Hepp and E. H. Lieb, *Ann. Phys. (NY)* **76**, 360 (1973).
- [9] Y. K. Wang and F. T. Hioe, *Phys. Rev. A* **7**, 831 (1973).
- [10] H. Carmichael, C. Gardiner, and D. Walls, *Phys. Lett. A* **46**, 47 (1973).
- [11] D. Nagy, G. Szirmai, and P. Domokos, *European Phys. J. D* **48**, 127 (2008).
- [12] K. Baumann, C. Guerlin, F. Brennecke, and T. Esslinger, *Nature (London)* **464**, 1301 (2010).
- [13] K. Baumann, R. Mottl, F. Brennecke, and T. Esslinger, *Phys. Rev. Lett.* **107**, 140402 (2011).
- [14] J. Klinder, H. Keßler, M. R. Bakhtiari, M. Thorwart, and A. Hemmerich, *Phys. Rev. Lett.* **115**, 230403 (2015).
- [15] M. R. Bakhtiari, A. Hemmerich, H. Ritsch, and M. Thorwart, *Phys. Rev. Lett.* **114**, 123601 (2015).
- [16] T. Flottat, L. de Forges de Parny, F. Hébert, V. G. Rousseau, and G. G. Batrouni, *Phys. Rev. B* **95**, 144501 (2017).
- [17] A. U. J. Lode and C. Bruder, *Phys. Rev. Lett.* **118**, 013603 (2017).
- [18] R. Lin, L. Papariello, P. Molognini, R. Chitra, and A. U. J. Lode, *Phys. Rev. A* **100**, 013611 (2019).
- [19] J. Léonard, A. Morales, P. Zupancic, T. Esslinger, and T. Donner, *Nature (London)* **543**, 87 (2017).
- [20] A. Morales, P. Zupancic, J. Léonard, T. Esslinger, and T. Donner, *Nature Mater.* **17**, 686 (2018).
- [21] F. Mivehvar, S. Ostermann, F. Piazza, and H. Ritsch, *Phys. Rev. Lett.* **120**, 123601 (2018).
- [22] F. Mivehvar, F. Piazza, and H. Ritsch, *Phys. Rev. Lett.* **119**, 063602 (2017).
- [23] A. U. J. Lode, F. S. Diorico, R. Wu, P. Molognini, L. Papariello, R. Lin, C. Lévéque, L. Exl, M. C. Tsatsos *et al.*, *New J. Phys.* **20**, 055006 (2018).
- [24] M. Landini, N. Dogra, K. Kroeger, L. Hruby, T. Donner, and T. Esslinger, *Phys. Rev. Lett.* **120**, 223602 (2018).
- [25] F. Mivehvar, H. Ritsch, and F. Piazza, *Phys. Rev. Lett.* **122**, 113603 (2019).
- [26] E. I. Rodríguez Chiacchio and A. Nunnenkamp, *Phys. Rev. Lett.* **122**, 193605 (2019).
- [27] V. D. Vaidya, Y. Guo, R. M. Kroeze, K. E. Ballantine, A. J. Kollár, J. Keeling, and B. L. Lev, *Phys. Rev. X* **8**, 011002 (2018).
- [28] E. J. Davis, G. Bentsen, L. Homeier, T. Li, and M. H. Schleier-Smith, *Phys. Rev. Lett.* **122**, 010405 (2019).
- [29] See Supplemental Material at <http://link.aps.org/supplemental/10.1103/PhysRevA.101.061602>, which further refers to Refs. [56, 57, 58, 59], for a description of the MCTDH-X algorithm, the system parameters, the derivation of the discretized-time

- mapping, the behaviors of the dimerization order parameter during the formation of double-well lattices, the hysteresis between SDSF and 2-SSF phases, the sensitivity of the strange attractors to the harmonic trap and atomic fluctuations, the behaviors of the system during thermalization, and the bifurcation related to the dynamical instabilities.
- [30] F. Piazza and H. Ritsch, *Phys. Rev. Lett.* **115**, 163601 (2015).
- [31] H. Keßler, J. G. Cosme, M. Hemmerling, L. Mathey, and A. Hemmerich, *Phys. Rev. A* **99**, 053605 (2019).
- [32] P. Zupancic, D. Dreon, X. Li, A. Baumgärtner, A. Morales, W. Zheng, N. R. Cooper, T. Esslinger, and T. Donner, *Phys. Rev. Lett.* **123**, 233601 (2019).
- [33] R. M. Kroeze, Y. Guo, V. D. Vaidya, J. Keeling, and B. L. Lev, *Phys. Rev. Lett.* **121**, 163601 (2018).
- [34] C. Maschler, I. B. Mekhov, and H. Ritsch, *Eur. Phys. J. D* **46**, 545 (2008).
- [35] D. Nagy, G. Kónya, G. Szirmai, and P. Domokos, *Phys. Rev. Lett.* **104**, 130401 (2010).
- [36] D. Nagy, G. Szirmai, and P. Domokos, *Phys. Rev. A* **84**, 043637 (2011).
- [37] F. Brennecke, R. Mottl, K. Baumann, R. Landig, T. Donner, and T. Esslinger, *Proc. Natl. Acad. Sci. USA* **110**, 11763 (2013).
- [38] F. Piazza, P. Strack, and W. Zwerger, *Ann. Phys. (NY)* **339**, 135 (2013).
- [39] F. Mivehvar, H. Ritsch, and F. Piazza, *Phys. Rev. Lett.* **118**, 073602 (2017).
- [40] A. U. J. Lode, *Phys. Rev. A* **93**, 063601 (2016).
- [41] O. E. Alon, A. I. Streltsov, and L. S. Cederbaum, *Phys. Rev. A* **77**, 033613 (2008).
- [42] E. Fasshauer and A. U. J. Lode, *Phys. Rev. A* **93**, 033635 (2016).
- [43] A. U. J. Lode, M. C. Tsatsos, E. Fasshauer, R. Lin, L. Papariello, P. Mognini, C. Lévêque, and S. E. Weiner, MCTDH-X: The time-dependent multiconfigurational hartree for indistinguishable particles software, 2020, <http://ultracold.org>.
- [44] R. Lin, P. Mognini, L. Papariello, M. C. Tsatsos, C. Lévêque, S. E. Weiner, E. Fasshauer, R. Chitra, and A. U. J. Lode, *Quantum Sci. Technol.* **5**, 024004 (2020).
- [45] A. U. J. Lode, C. Lévêque, L. B. Madsen, A. I. Streltsov, and O. E. Alon, *Rev. Mod. Phys.* **92**, 011001 (2020).
- [46] R. J. Glauber, *Phys. Rev.* **130**, 2529 (1963).
- [47] K. Sakmann, A. I. Streltsov, O. E. Alon, and L. S. Cederbaum, *Phys. Rev. A* **78**, 023615 (2008).
- [48] M. Greiner, O. Mandel, T. Esslinger, T. W. Hänsch, and I. Bloch, *Nature (London)* **415**, 39 (2002).
- [49] S. Wessel, F. Alet, M. Troyer, and G. G. Batrouni, *Phys. Rev. A* **70**, 053615 (2004).
- [50] Y. Kato, Q. Zhou, N. Kawashima, and N. Trivedi, *Nat. Phys.* **4**, 617 (2008).
- [51] M. Jääskeläinen and P. Meystre, *Phys. Rev. A* **71**, 043603 (2005).
- [52] A. Wagner, A. Nunnenkamp, and C. Bruder, *Phys. Rev. A* **86**, 023624 (2012).
- [53] S. H. Strogatz, *Nonlinear Dynamics and Chaos* (Perseus, Cambridge, MA, 1994).
- [54] A. A. Andronov, E. A. Leontovich, I. J. Gordon, and A. G. Maier, *Theory of Bifurcations of Dynamical Systems on a Plane* (Israel Program Sci. Transl., Jerusalem, 1971).
- [55] J. Klinder, H. Keßler, M. Wolke, L. Mathey, and A. Hemmerich, *Proc. Natl. Acad. Sci. USA* **112**, 3290 (2015).
- [56] P. Kramer and M. Saraceno, *Geometry of the Time-Dependent Variational Principle in Quantum Mechanics*, Lecture Notes in Physics Vol. 140 (Springer, Berlin, 1981).
- [57] A. U. J. Lode, K. Sakmann, O. E. Alon, L. S. Cederbaum, and A. I. Streltsov, *Phys. Rev. A* **86**, 063606 (2012).
- [58] J. I. Neimark, *Dokl. Akad. Nauk SSSR* **129**, 736 (1959).
- [59] R. J. Sacker, On invariant surfaces and bifurcation of periodic solutions of ordinary differential equations, Technical Report No. IMM-NYU 333, New York University, 1964.